Numerical Modelling of a Metal Vapour Flow inside a Vapour Distribution Box

M.C. Roebroeck

Technische Universiteit Delft

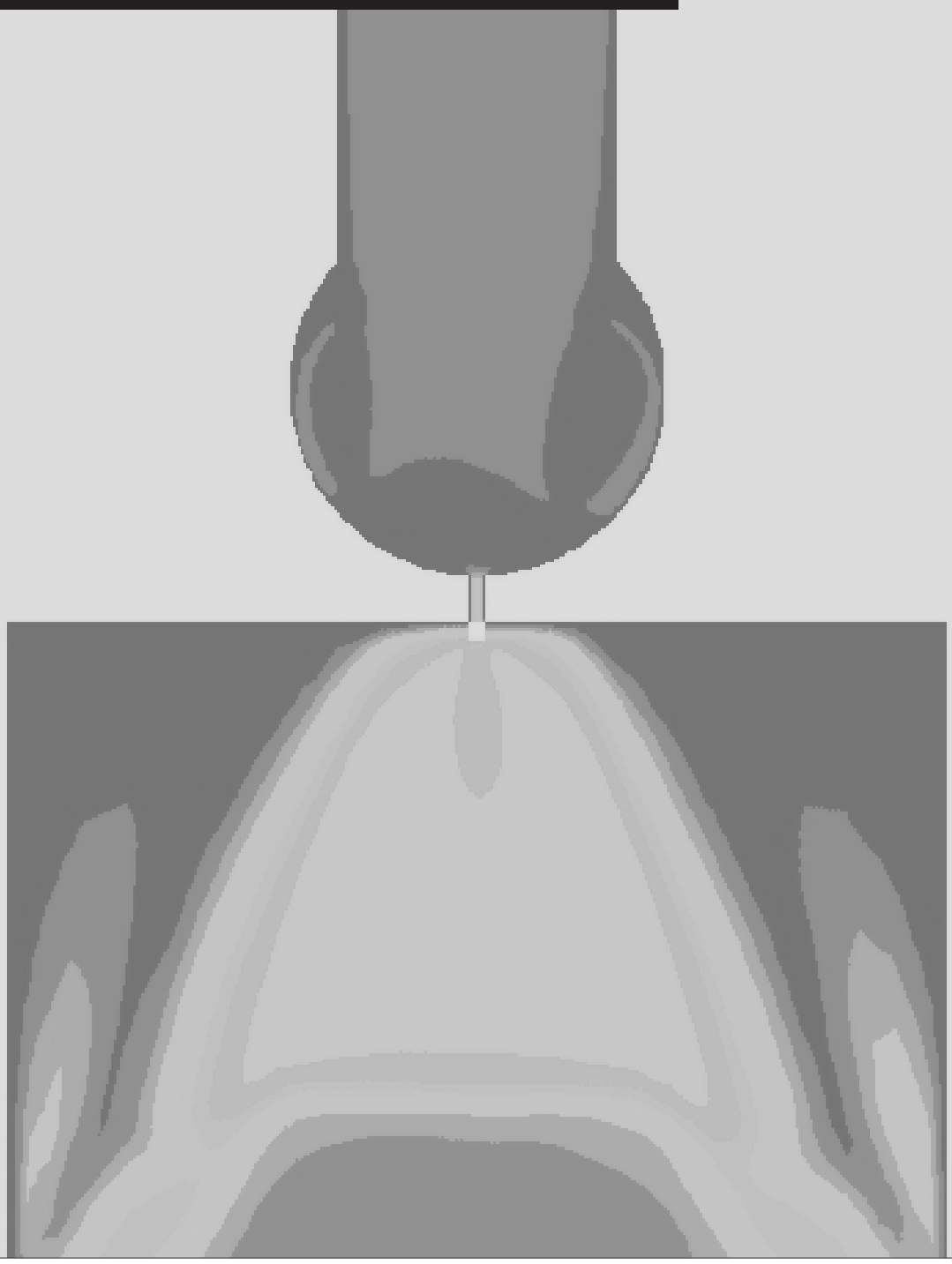

TU Delft Delft University of Technology

Challenge the future

Numerical Modelling of a Metal Vapour Flow inside a Vapour Distribution Box

by

M.C. Roebroeck

in partial fulfillment of the requirements for the degree of

Bachelor of Science
in Molecular Science and Technology

at the Delft University of Technology
Research group Transport Phenomena

Supervisors: Prof. dr. ir. C.R. Kleijn
Dr. ing. S. Kenjeres
J.E. Vesper MSc.

TU Delft Delft University of Technology

Contents

1 Introduction **1**

2 Research Objective **3**
2.1 Numerical methods and physical properties . . . 3
2.2 Mesh dependency study . . . 3
2.3 Results of the first version of the model . . . 3

3 Theory **5**
3.1 Conservation equations . . . 5
3.2 Discretisation schemes . . . 6
3.3 Dimensionless numbers . . . 8
3.4 Streamlines . . . 9

4 Numerical methods and physical properties **11**
4.1 Compressibility effects . . . 11
4.2 Physical properties and solver settings . . . 11
4.2.1 Physical properties . . . 11
4.2.2 Solver settings . . . 13

5 Mesh dependency study **15**
5.1 Method . . . 15
5.1.1 Geometry of the vapour distribution box . . . 16
5.1.2 Geometry of the mesh . . . 16
5.1.3 Mesh criteria . . . 17
5.1.4 Mesh types . . . 18
5.1.5 Number of elements . . . 18
5.2 Final meshes . . . 19

6 Results of the first version of the model **21**
6.1 Pressure and velocity contours . . . 21
6.2 Lateral distribution of mass outflow over the slit . . . 24
6.3 Temperature pressure diagram to analyse in which regions the phase state is above or below the vapour pressure curve . . . 25
6.4 The influence of different slit widths . . . 27

7 Conclusion and recommendations **31**
7.1 Conclusions . . . 31
7.2 Recommendations . . . 32

A Appendix: User Defined Function **33**

Bibliography **35**

1

Introduction

Steel is a commonly used material, each year approximately 1500 million tons of steel are used all over the world [1]. To extend the lifespan of steel, avoid corrosion or obtain desired surface properties, steel is coated. There are many different steel coating processes, one of which is Physical Vapour Deposition (PVD)[2]. PVD has a high flexibility regarding coating thickness and composition. Furthermore, the energy consumption for this method is low and the waste stream is limited compared to currently used coating processes such as Chemical Bath Deposition where a bath of liquid metal is used to deposit thin films. PVD as a new way of coating is more sustainable and therefore of interest to steel companies.

The coating of steel with PVD is a continuous process, which requires the steel to be exposed to multiple vapour jets at a high mass flow rate. This high mass flow rate can be achieved by using a Vapour Distribution Box (VDB). At the inlet, shown in figure 1.1, the source material, solid zinc, is heated until the boiling point is reached. The rising zinc vapour is directed through a vapour deposition chamber into a vacuum chamber, where it is deposited on the substrate, the steel plate, through the nozzles, which are simulated in this research as one slit. An overview of this process is shown in figure 1.2.

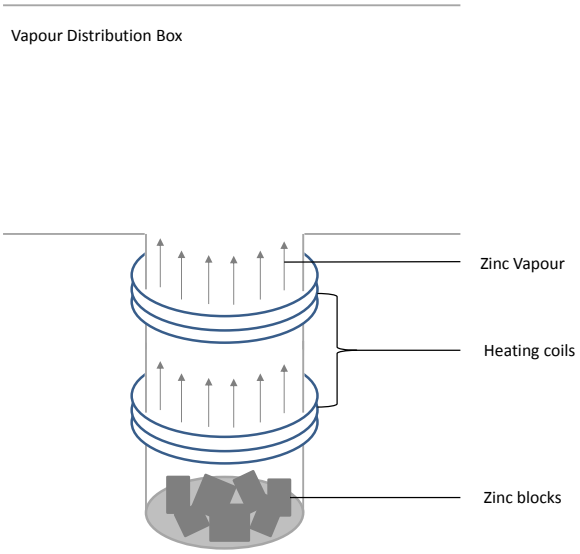

Figure 1.1: Inlet of the Vapour Distribution Box

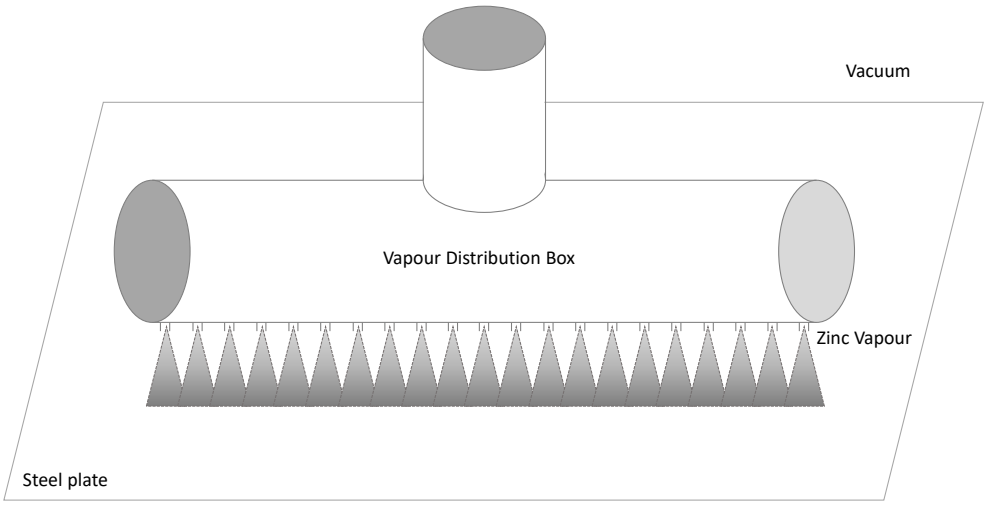

Figure 1.2: Overview over the Physical Vapour Deposition process

A problem encountered during this process is that in the zinc vapour flow little droplets may occur. These droplets disturb the coating process, causing unevenness in the coating instead of creating a smooth and flat layer. This could potentially affect the position on the sales market and later on this unevenness could cause problems with further processing.

To find a solution to this problem research needs to be performed on the origin of these droplets, their path and the reason why the droplets are reaching the substrate, without colliding with the wall of the distribution box.

This report will focus on creating a numerical model to give insight into the physics of the flow process inside the chamber, which later on can be compared to experimental results.

The research objective is stated in chapter 2. The theoretical background is given in chapter 3. Chapter 4 will elaborate on all other model inputs like psychical properties, boundary conditions and solutions methods. Chapter 5 will elaborate on the mesh that is used in the numerical model. In chapter 6 the results of the first version of the model are analysed using different input variables. Finally, in chapter 7 the outcomes of chapter 4, 5 and 6 are discussed and conclusions and recommendations for further research will be given.

2

Research Objective

The research objective is to create and optimize a numerical model, based on the ANSYS Fluent computational fluid dynamics (CFD) code, to simulate the flow inside a vapour distribution box as part of the physical vapour deposition process. This objective is divided into three different parts:

2.1. Numerical methods and physical properties

The numerical methods used by ANSYS Fluent must be appropriate. The most suitable solving method must be determined as well as the correct physical properties and boundary conditions.

2.2. Mesh dependency study

The main target of this mesh dependency study is to build a representative mesh. An iterative process is applied, starting with the most simple mesh types. The final mesh can be used as a reliable base for further research.

2.3. Results of the first version of the model

The first version of the model will be evaluated by analysing the following items:

- Pressure and velocity contours
- Lateral distribution of mass outflow over the slit outlet
- Temperature pressure diagram to analyse in which regions the phase state is above or below the vapour pressure curve
- The influence of different slit outlet widths

3

Theory

This chapter will be an introduction to the relevant theory. Section 3.1 will give an overview over the governing equations. Afterwards, a short introduction to the different discretization schemes will be made in section 3.2. Section 3.3 will give an overview over the research related dimensionless numbers. Additionally, section 3.4 will be about the definition of streamlines.

3.1. Conservation equations

In the system the conservation of mass, momentum and energy need to be taken into account. The governing equations are therefore the continuity equation, the Navier-Stokes equations and the energy equation.

The change in **mass** over time is equal to the mass entering the system minus the mass leaving the system plus the mass production in the system. The general mass balance is described by

$$\frac{d}{dt}M = \phi_{m,in} - \phi_{m,out} + P \ , \tag{3.1}$$

where t is the time, M the mass, ϕ_m the mass flow in and out and P the production.

The material derivative describes the change of a physical quantity, ϕ, exposed to a time dependent and space dependent variational velocity vector field, in time. The material derivative can be used to couple the Eulerian and Lagrangian descriptions of continuum deformation. The **material derivative** is described in cartesian coordinates as

$$\frac{d\phi}{dt} = \frac{\partial \phi}{\partial t} + v_i \frac{\partial \phi}{\partial x_i} \ , \tag{3.2}$$

where i is a n index, as the studied geometry has three dimensions, $i \in x, y, z$.

The **continuity** equation describes the mass conservation

$$\frac{\partial \rho}{\partial t} + \frac{\partial \rho v_i}{\partial x_i} = 0 \ . \tag{3.3}$$

The divergence $\frac{\partial v_i}{\partial x_i}$ is zero for an incompressible flow. If the Mach number is greater than 0.3, the density of a fluid element may undergo a high change, so that the assumption of divergence free flow, i.e. incompressibility is not justifiable.

The conservation equation of **momentum** is equal to the momentum flow entering the system minus the momentum flow leaving the system plus the production of momentum created by three different forces, the body force, e.g. gravity, the pressure force and the shear forces. For only the x direction one can write

$$\frac{d}{dt}(Mv_x) = \phi_{m,in} v_{x,in} - \phi_{m,out} v_{x,out} + \sum F_x \ . \tag{3.4}$$

In general the Navier-Stokes equations describe a motion of viscous fluids. The compressible form in Cartesian coordinates, using the index notation, can be described as

$$\frac{\partial \rho v_i}{\partial t} + \frac{\partial (\rho v_i v_j)}{\partial x_j} = -\frac{\partial p}{\partial x_i} + \frac{\partial}{\partial x_j}\left(\mu\left(\frac{\partial v_i}{\partial x_j} + \frac{\partial v_j}{\partial x_i} - \frac{2}{3}\frac{\partial v_k}{\partial x_k}\delta_{ij}\right)\right) + \rho f_i \ , \tag{3.5}$$

where the terms present from left to right, the temporal term, the convective term, the pressure gradient, the viscous term and the body force term.

The conservation of **Energy** is described in the following equation

$$\frac{\partial \rho E}{\partial t} + \frac{\partial (v_j(\rho E + p))}{\partial x_j} = \frac{\partial}{\partial x_j}\lambda\frac{\partial T}{\partial x_j} + \rho\Gamma + \frac{\partial(\tau_{ij}v_i)}{x_j} \ . \tag{3.6}$$

The dissipation is very small and therefor negligible. Γ is the radiation, τ_{ij} is the anisotropic stress given by $\mu\left(\frac{\partial v_i}{\partial x_j} + \frac{\partial v_j}{\partial x_i} - \frac{2}{3}\frac{\partial v_k}{\partial x_k}\delta_{ij}\right)$.

The energy E is given by

$$E = h - \frac{p}{\rho} + \frac{v^2}{2} \ , \tag{3.7}$$

$h - \frac{p}{\rho}$ is the internal energy where the h is the enthalpy and p/ρ the pressure energy. $\frac{v^2}{2}$ is the specific kinetic energy.

The above equations cannot be solved exactly and therefore the equations need to be discretized to solve it numerically. The FVM is used for the discretization. Here we show this procedure for the Navier-Stokes equations. Equation 3.5 is integrated over a control volume in the computational cell yielding

$$\iiint_{CV}\left(\frac{\partial \rho v_i}{\partial t} + \frac{\partial \rho v_i v_j}{\partial x_j}\right)dV = \iiint_{CV}\left(-\frac{\partial p}{\partial x_i} + \frac{\partial}{\partial x_j}\left(\mu\left(\frac{\partial v_i}{\partial x_j} + \frac{\partial v_j}{\partial x_i} - \frac{2}{3}\frac{\partial v_k}{\partial x_k}\delta_{ij}\right)\right) + \rho f_i\right)dV \ . \tag{3.8}$$

In the FVM, the Gauss' divergence theorem is used to convert volume integrals containing a divergence term into surface integrals. The temporal term and source terms are assumed constant over the cell's volume.

$$\frac{\partial \rho v_i}{\partial t}V + \iint_A \rho v_i v_j n_j dA = -\iint_A p n_i dA + \iint_A \mu\left(\frac{\partial v_i}{\partial x_j} + \frac{\partial v_j}{\partial x_i} - \frac{2}{3}\frac{\partial v_k}{\partial x_k}\delta_{ij}\right)n_j dA + \rho f_i V \tag{3.9}$$

This surface integrals can be written as a summation over all the faces, referred as f, of the computational cell

$$\frac{\partial \rho v_i}{\partial t}V + \sum_f (\rho v_i v_j n_j A)_f = -\sum_f (\rho p n_i A)_f + \sum_f \left(\mu\left(\frac{v_i}{x_j} + \frac{\partial v_j}{\partial x_i} - \frac{2}{3}\frac{\partial v_k}{\partial x_k}\delta_{ij}\right)n_j A\right)_f + \rho f_i V \ . \tag{3.10}$$

3.2. Discretisation schemes

Discretisation is the process of transferring a continuum into a finite set of points, in other words replacing the continuous function into discrete counterparts. This can be done using a finite differencing method or using a Finite Volume Method (FVM). In this research the FVM is used. For this method the domain is divided up into smaller volumes, control volumes. The centre of these control volumes are held representative for the value over the entire control volume. By integrating the partial differential equation over the control volume the equation is fitted into a form that ensures conservation. The derivatives at the faces of the cell are approximated by a finite differencing scheme and a system of sparse linear equation is generated that can be solved using a standard linear method[3, chapter 2]. Different differencing schemes can be used and are explained on the basis of the simplification of a 2D cell structure, as shown in figure 3.1.

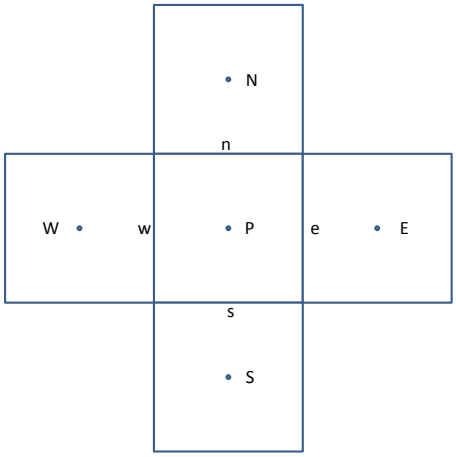

Figure 3.1: A simplified scheme of five cells next to each other. The capital letters indicates the cell centres and the lower case variants demote the values at the respective faces

Central differencing scheme

One of the second order differential schemes is the Central Differencing Scheme (CDS). To calculate the quantity values at the faces of a computational cell an linear interpolation of the cell centres values is used. Using the simplified scheme of figure 3.1, as an example one can write

$$\phi_W = \frac{\phi_P - \phi_W}{2} \tag{3.11}$$

as a scalar or,

$$\left(\frac{\partial \phi}{\partial x}\right)_w = \frac{\phi_P - \phi_W}{\delta x} \tag{3.12}$$

as a gradient where ϕ presents any scalar quantity. In figure 3.2 the scheme is shown.

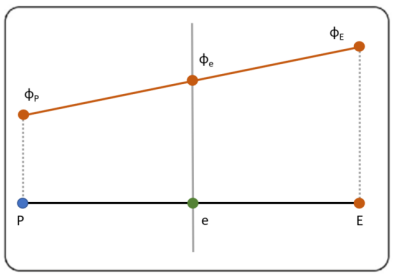

Figure 3.2: Central Differencing Scheme - Face interpolation [4]

Upwind differencing scheme

The central differencing scheme is useful, e.g. for diffusive terms, however in some cases the upwind differencing scheme is needed. By taking the flow direction into account the upwind differencing scheme uses the value from the center of the cell as the value at the face of the cell. Using the first order upwind scheme result in the following equations: For a positive flow direction, $u_x > 0$

$$\begin{cases} \phi_e = \phi_P \\ \phi_w = \phi_W \end{cases}. \tag{3.13}$$

For a negative flow direction, $u_x < 0$

$$\begin{cases} \phi_e = \phi_E \\ \phi_w = \phi_P \end{cases} . \tag{3.14}$$

In figure 3.3 the scheme is pictured.

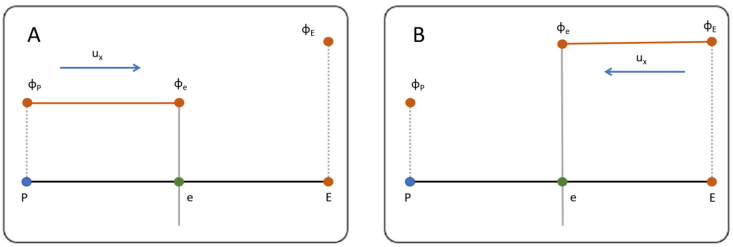

Figure 3.3: Upwind Differencing Scheme - Face interpolation [4]

3.3. Dimensionless numbers

The following dimensionless numbers are important to this research

The **Reynolds** number gives a prediction of the nature of the flow pattern, viz. whether it is laminar or turbulent.

$$Re = \frac{v\rho L}{\mu} = \frac{vL}{\nu} = \frac{inertia\,forces}{viscous\,forces} \tag{3.15}$$

In the VDB the viscous forces are relatively high. This is caused by for example the high temperature. This results in a low Reynolds number. The expectation is therefore a laminar flow. However, the Reynolds number will be close to the tipping point between a laminar flow and a turbulent flow. This research will explore whether the flow is laminar as expected.

The **Mach** number is representing the ratio between the flow velocity and the speed of sound. The Mach number will tell whether the flow is supersonic. A flow is supersonic if the Mach number is above one, which means that the local flow velocity is higher than the speed of sound within the medium. If a flow is supersonic, one can assume that no information is able to travel back.

$$M = \frac{u}{a} = \frac{u}{\sqrt{\kappa \frac{p}{\rho}}} = \frac{the\,local\,flow\,velocity\,with\,respect\,to\,the\,boundaries}{the\,speed\,of\,sound\,in\,the\,medium} , \tag{3.16}$$

where κ is the isentropic expansion factor of a real gas $\kappa = \frac{C_p}{C_v}$. Since the studied Zinc vapour is a monatomic gas, there are three degrees of freedom: $\kappa = 1 + \frac{2}{f} = \frac{3}{3} + \frac{2}{3} = \frac{5}{3} = 1.67$. Since $\frac{p}{\rho}$ is hard to calculate, it can be replaced by $R_M T$. If one inserted $V = \frac{Mn}{\rho}$ in $PV = nRT$, results in $\frac{P}{\rho} Mn = nRT$ and thus $\frac{P}{\rho} = \frac{RT}{M} = R_M T$.

The **Knudsen** number tells whether statistical mechanics or a continuum mechanic formulation of fluid dynamic should be used for modelling a situation. The Knudsen number is defined as follows:

$$Kn = \frac{\lambda}{L} = \frac{the\,mean\,free\,path}{the\,characteristic\,length} , \tag{3.17}$$

$$\text{where } \lambda = mean\,free\,path = \frac{1}{\sqrt{2}\pi n d^2} . \tag{3.18}$$

d is the collisional diameter which is for zinc, $d_{zinc} = 5,684 \times 10^{-10}$m [5] and n is here the number density defined as shown in equation 3.19.

$$n = \frac{p}{k_b T} , \tag{3.19}$$

where p is the total pressure, k_b is the Boltzmann constant and T the thermodynamic temperature.

If the mean free path of a molecule is comparable to a length scale of the problem, the Knudsen number is greater than one and the continuum mechanics formulation is no longer useful.

A **relationship between these dimensionless numbers** can be set up using the expression for dynamic viscosity shown in equation 3.20 and the expression for the average molecular speed shown in equation3.21.

$$\mu = \frac{1}{2}\rho\bar{c}\lambda \tag{3.20}$$

$$\bar{c} = \sqrt{\frac{8k_bT}{\pi M}} \tag{3.21}$$

If equation 3.21 is inserted in equation 3.20, the λ is withdrawn and the characteristic length term is added, the relationship between the three dimensionless numbers can be described as

$$Kn = \frac{Ma}{Re}\sqrt{\frac{\kappa\pi}{2}} \approx 1.62\frac{Ma}{Re}\ . \tag{3.22}$$

3.4. Streamlines

There are multiple ways used to visualize CFD simulations of a fluid flow. A difference is made between streamlines, streaklines and pathlines. Yet in a steady flow these terms coincide [6]. Since in this report the steady case is researched, only the definition of streamlines will be explained.

Streamlines are a set of curves that coincide with the direction of the tangent line of the velocity vector of the flow field. It displays in which direction at any point in time a fluid element flows. The streamlines are calculated directly from the instantaneous velocity flow field.

Streamlines are defined by

$$\frac{d\vec{x}_S}{ds} \times \vec{v}(\vec{x_S}) = 0, \tag{3.23}$$

where $\vec{x_S}(s)$ presents one streamline parameter at one moment in time, $\vec{v}$ the velocity vector at the same moment in time and $\times$ stands for the vector cross product [7].

When the vectors are described in components, $\vec{v} = (v_x, v_y, v_z)$ and $\vec{x_S} = (x_S, y_S, z_S)$, one can derive

$$\frac{dx_S}{v_x} = \frac{dy_S}{v_y} = \frac{dz_S}{v_z}\ . \tag{3.24}$$

This equation, 3.24, confirm the parallelism of the velocity vector and the calculated streamline.

4

Numerical methods and physical properties

In ANSYS Fluent 17.1 [8] all boundary conditions for the flow and energy equations need to be specified. The physical properties of the fluid need to be set up, all different models need to be looked into and the solution methods need to be chosen. In this chapter the numerical method and physical properties are discussed. The domain set up will be discussed in the following chapter, chapter 5.

4.1. Compressibility effects

The flow is compressible and this can lead to difficulties caused by a high degree of coupling between the flow velocity, density and energy. The iterative numerical solution process can be disturbed by this coupling and therefore not converge. Not only the coupling can disturb the reach of convergence, the presence of shocks can cause a stability problem as well. The following steps should be taken to solve the divergence problem: [9, chapter 8.4.5]

- Limit the temperature and pressure especially for the first iterations
- Take a reduced pressure ratio at the boundaries for the first iterations
- Start the compressible flow calculation from an incompressible flow solution
- Start computing with an inviscid solution

4.2. Physical properties and solver settings

Giving proper initial conditions and a set of boundary conditions is crucial for the results. Little deviation could have major effects on the results. The flow in the VDB is compressible[10]. Compressibility effects like the local change of density, occur because of a flow velocity exceeding the speed of sound of the gas, Mach>0.3, see equation 3.16. The pressure gradient is large as well [9, chapter 1.6].

4.2.1. Physical properties

Operating pressure

The operating pressure is defined by $P_{op} = P_{abs} - P_{gauge}$. In this research there is no atmospheric/hydrostatic pressure, since the process takes place in a vacuum chamber so the gauge pressure is equal to the absolute pressure. Since the ideal gas law is used to determine the density and the Mach number will be >0.1, the operating pressure is set to zero.

Flow model

The Reynolds number of the flow is small, order-size 500, so that no turbulence model is required and a laminar flow will succeed.

Density
The density is calculated from the ideal-gas law, using a molar mass of M = 65.38 g/mol.

Specific heat capacity
The molar heat capacity at a constant volume of the gas, $C_{V,m} = \frac{5}{2}R$, for temperatures between 500 K and 1000 K [11]. For zinc-vapour the molar heat capacity is therefore $20.79\frac{J}{molK}$. Transferring the molar heat capacity into the specific heat capacity will give $C_p = 318\frac{J}{kgK}$

Thermal conductivity
The thermal conductivity used is, $\lambda = 0.0242\frac{W}{mK}$. This is the thermal conductivity for air. Zinc vapour should have a lower thermal conductivity but this will be close enough for creating a first approximation.

Viscosity
For the viscosity a piece-wise linear relation is used since the viscosity vary with $\sqrt{T}$. The two points given are:

Temperature (K)	Viscosity (kg/m s)
673.15	1.63×10^{-05}
1273.15	2.79×10^{-05}

Table 4.1: Points taken for the piece-wise linear relation for the viscosity of zinc vapour

Boundary conditions
Figure 4.1 shows a sketch of the studied geometry, with the different parts of the boundaries indicated. All inputs for pressure are relative to the operating pressure and all temperature inputs at the inlet are total temperatures, not static temperatures.

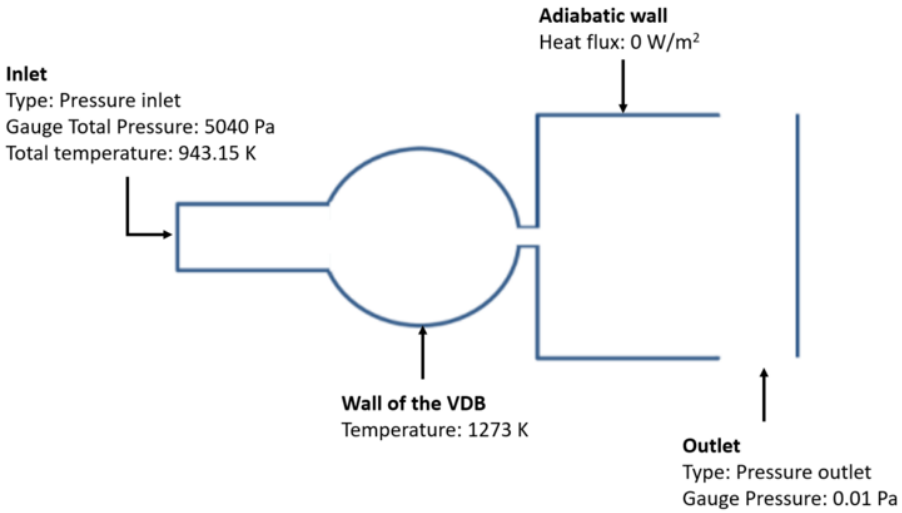

Figure 4.1: Boundary conditions

The inlet conditions are given. The temperature of the wall of the VDB is 1273 K. This is the measured temperature at these walls. The same reason goes for having no heat flux at the adiabatic wall. The vacuum outlet is approached by taking a pressure of 0.01 Pascal. To reach convergence with this high pressure gradient the outlet pressure was first set at 1000 Pascal and the data output was used as an input when decreasing this outlet temperature.

4.2.2. Solver settings

The problem is steady-state since all variables which have influence on the behavior of the system are time independent. The two solver types, pressure-based and density-based are compared. The outcomes of these two solver must not differ and, as can be seen in figure 4.2 and 4.3, the two solvers show a high similarity. However, the expectation is that a density-based solver is more suitable since the pressure gradient is high as well as the operating temperature. In a density-based solver the governing equations, i.e. the continuity, momentum, and energy conservation equation, are solved simultaneously instead of sequentially. However, governing equations for additional scalars, for example turbulence and radiation will be solved sequentially.

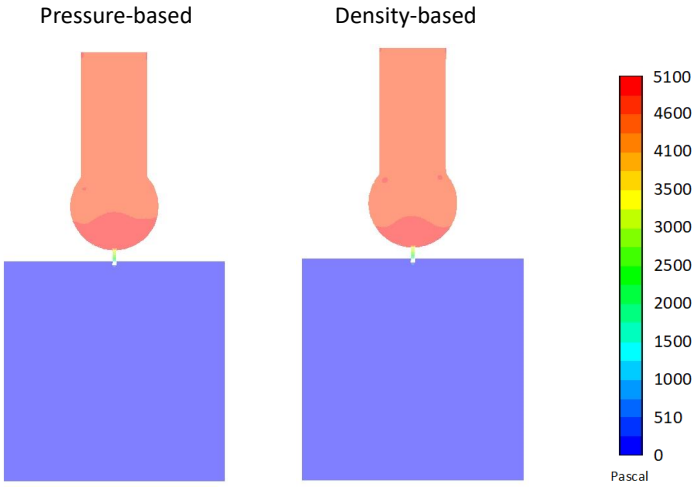

Figure 4.2: Static pressure contours

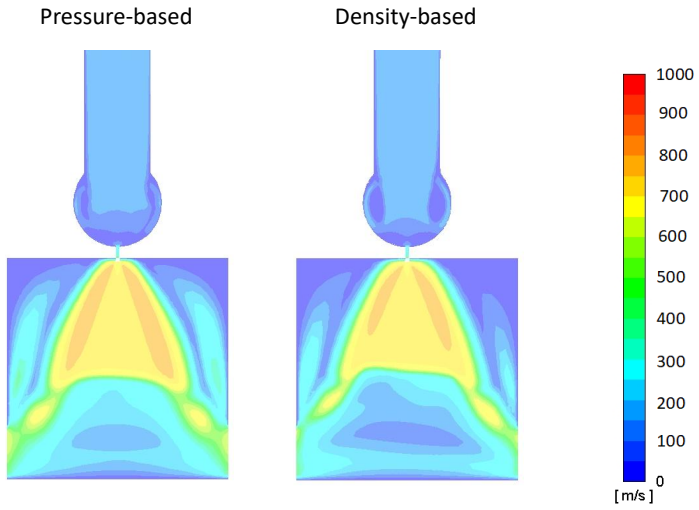

Figure 4.3: Velocity magnitude contours

The different discretization scheme have been explained in chapter 3, section 1. Since the physical diffusion is smaller than the convection the central differencing scheme is not suitable. The Upwind scheme is developed for strong convective flows with suppressed diffusion effects. Since this matches our case the upwind scheme is used.

The system consists of five governing equations mentioned in chapter 3, section 2. This system itself can not be solved directly since all equations are depending on each other. Besides, there is one non-linear term in the system. This is the convective term in the Navier-Stokes equation. This term needs to be linearised. To solve the system a pressure correction method is needed. The pressure-correction method using the SIMPLE (Semi-Implicit Method for pressure linked equations) algorithm is explained by the following figure 4.4:

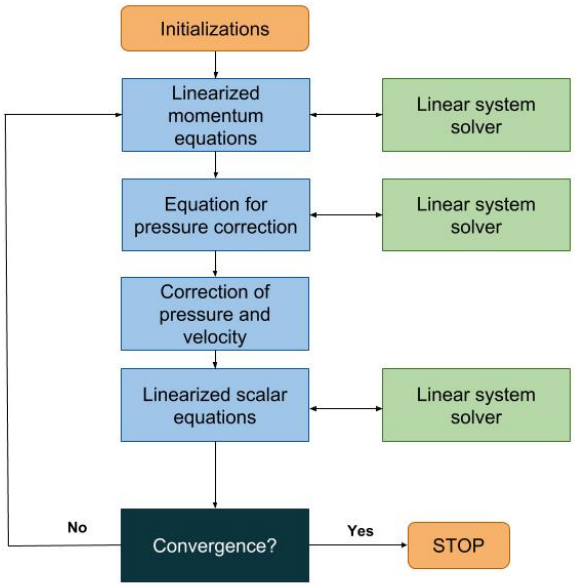

Figure 4.4: Steps simple method [12]

In the first step the linearised discretised momentum equations are solved using an estimated value for the pressure field, p*. This either could be the pressure field from the previous iteration or just take a starting value of zero. The velocity components u*,v* and w* are determined, but do not fulfill the continuity equation. Inserting the values of u*, v* and w* in the continuity equation results in a residual mass source, b_m. By respective substraction of the three linear momentum equations and the mass balance from the five governing equations, new relations are set up where the sum terms are neglected. This approach yields the SIMPLE method. Step two: A linear equation system is set up from which the pressure correction p' can be determined. The correction is defined by $p' = p^{n+1} - p*$ where n+1 is representing the next iteration. Step three: using p' the values for u', v' and w' can be determined. With these values the searched quantities u^{n+1}, v^{n+1}, w^{n+1} and p^{n+1} can be calculated. In the last step all additional scalars can be determined. If all new values fulfill the momentum equations as well as the continuity equation the solution is converged, if not the values of iteration n+1 are used as initial values for the next iteration and the linearised momentum equations need to be solved again.

5

Mesh dependency study

The research in this report was conducted using computational fluid dynamics software. ANSYS ICEM CFD 17.1 [13] was used for setting up the geometry and creating a mesh. Meshes represent a geometric object as a set of finite elements. There are different mesh types, such as the examples shown in figure 5.1. The geometry is split into a certain number of elements of different types. The first mesh for this research will be made from the most simple mesh type and from there on an iterative process will start until the most suitable mesh is found. Besides the mesh type, also the number of elements in the mesh can determine whether a mesh is suitable for the case or not. If the number of elements is large, a lot of computing capacity is needed. Therefore a low density mesh will be created to start with. Increasing the fineness of this low density mesh will lead to more accurate results but this will take more calculation time. The research objective is to design a mesh with a low number of elements giving sufficiently accurate results. The result is a mesh-file as shown in figure 5.1. The domain extends and the volume statistics and the face area statistics are set and can be used as a reliable base for further research.

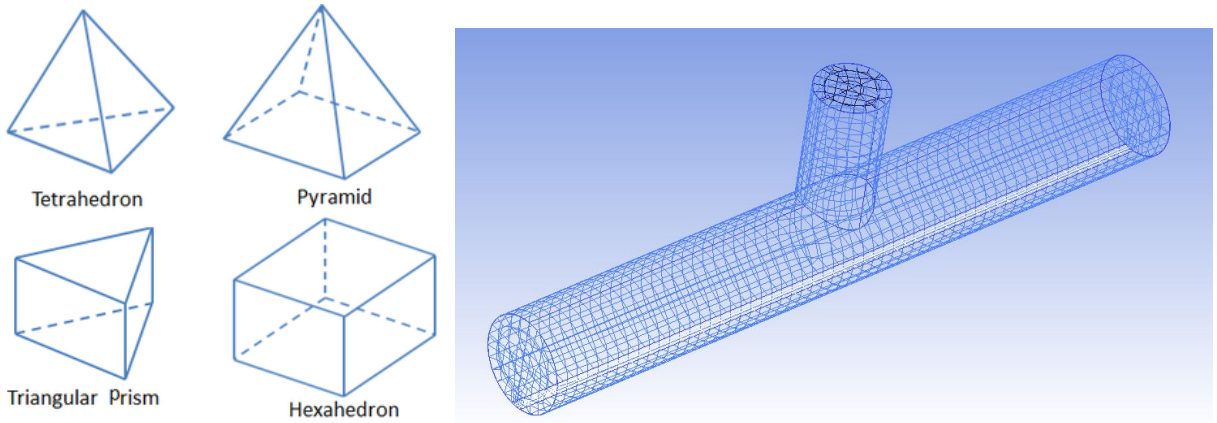

(a) Different mesh types [14]

(b) Mesh file

Figure 5.1: Meshing in ANSYS ICEM CFD

5.1. Method

The method is divided in five subsections. The dimensions of the VDB are given, the method to design the dimensions and geometry of the mesh is elaborated upon, the method to criticize the mesh, the method on how to choose the mesh type and the number of elements of the mesh.

5.1.1. Geometry of the vapour distribution box

In the following figure, 5.2, the geometry of the VDB is shown. This geometry is set up on the basis of two patents [15][16]. The inlet is a cylindrical box with a radius of 15 mm. This cylinder is in a 90 degree angle with a second cylinder. The horizontal distribution cylinder has a radius of 20 mm and a length of 300 mm. At the bottom of this cylinder multiple nozzles are placed. Each nozzle is assumed to have a diameter of 3 mm and the distances between the nozzles is 12 mm. In the real life situation this picture has to be turned 180 degrees around the x-axis. This has no influence on the results, as the process takes place in a vacuum chamber and the effect of gravity on the low density fluid is negligible compared to the driving pressure gradient.

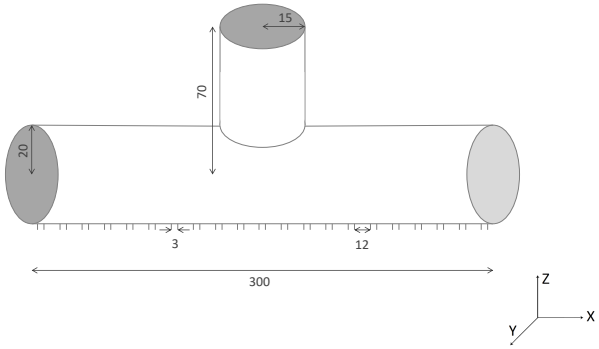

Figure 5.2: Geometry of the VDB in mm

5.1.2. Geometry of the mesh

The high number of cells required to discretise the nozzles would yield an immense computational cost. Therefore, the geometry is simplified. As described above the outlet consists of multiple nozzles. In the simplified geometry these nozzles are replaced by a single slit. This slit includes the whole x-direction. Three different slit widths will be compared in this research and therefore the different geometries are made.

The simplified geometry has undergone an iterative process. The first geometry was just the VDB with a slit outlet. Due to inconvenient boundary conditions at the outlet the conservation equations are not easily solved. To create far distant boundary conditions a virtual box was placed underneath the slit. The boundaries of this box represented the outlet. The third geometry was created due to the reversed flow at the walls of the box. To prevent this reversed flow from occurring the box is opened up at the vertical sides of the bottom. These open sides were set as outlet. The rest of the box were set as walls. This evolution of the geometry is shown in figure 5.3.

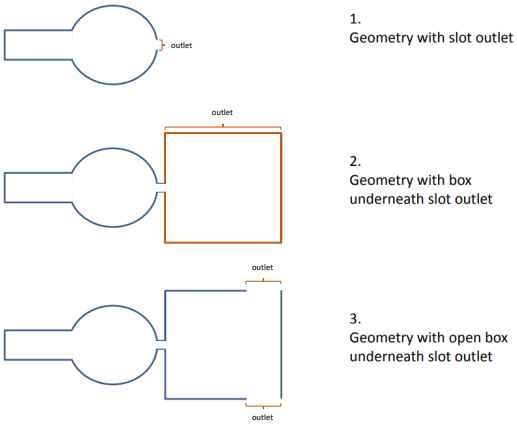

Figure 5.3: The evolution steps of the mesh with plane coordinates (0.15;0;0)

5.1.3. Mesh criteria

To determine whether the mesh is completed and suitable for further research it is tested on the basis of a number of criteria [17, chapter 15.3.2], which are explained below

- The orthogonality is approaching 1.
- The aspect ratio is below 1000.
- Each part must have at least three elements in each direction.

The orthogonality of the mesh is set in a range from 0 to 1. The angles between adjacent element faces or adjacent element edges are compared to an optimal angle. For triangular faced elements this optimal angle is 60° and for quadrilateral faced elements this optimal angle is 90°. The closer the angle of the adjacent element faces of edges is to the optimal angle the closer the orthogonality is to one. The most relevant measure of mesh orthogonality involves the angle between the vector that joins two mesh nodes and the normal vector for each integration point surface associated with that edge, shown in figure 5.4. It depends on the discretization scheme whether the chosen criteria number is sufficient. Using upwind discretization scheme the orthogonality needs to be higher than 0.5 in each element and the mean of orthogonality needs to be higher than 0.8.

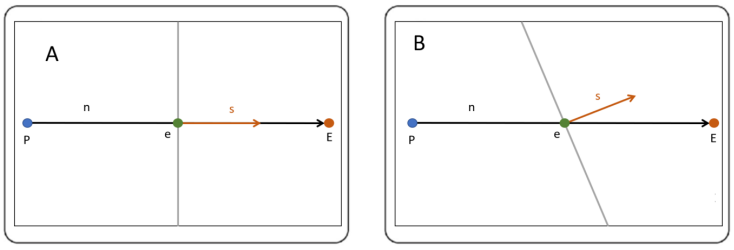

Figure 5.4: A: orthogonal mesh B: non-orthogonal mesh [4]

The aspect ratio of a geometric shape is an expression which tells something about the ratio of its sizes in different dimensions. The aspect ratio in case of a mesh involves the ratio of the maximum to minimum integration point surface areas in all elements. The more an element is stretched the higher the aspect ratio. For running double precision the acceptable range for the aspect ratio is below 1000. In figure 5.5 is shown how the aspect ratio is calculated for a tetra-shaped and a hexahedron-shaped volume[18].

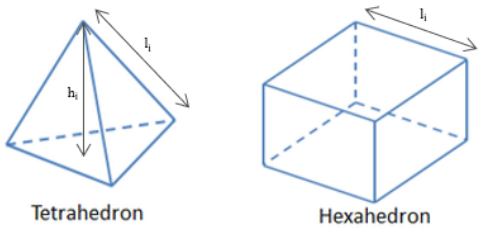

$$\text{Aspect ratio} = \frac{\sqrt{3}}{\sqrt{2}} \frac{\text{Min}\,(h_i)}{\text{Min}\,(l_i)} \qquad \text{Aspect ratio} = \frac{\text{Min}\,(l_i)}{\text{Max}\,(l_i)}$$

Figure 5.5: Aspect ratio for different mesh types

Each part of the computational domain needs to contain a minimum amount of three elements for each direction. When there are only one or two cells the calculations over this part are not accurate enough.

5.1.4. Mesh types

To determine the mesh type an iterative approach was used. The first mesh consisted of the easiest-to-build mesh type, tetrahedral. A tetrahedron mesh can be automatically generated with a meshing tool. In the end the hexahedral mesh type was used. For this type the standard meshing category is not suitable and therefore the blocking category was used. Creating a mesh by blocking is more difficult, but the benefit of this type is that for the same cell amount, the accuracy of solutions in hexahedral meshes is the highest. Less iterations are needed to reach convergence when using the same case.

5.1.5. Number of elements

The higher the number of elements in a mesh the more time it takes to calculate towards the solution. A balance needs to be found between the accuracy of the results and the run time. To conclude which number of elements suffices the total mass flow at the slit (ϕm) is plotted versus the number of elements, see figure 5.6. The refinement of the mesh has only taken place in the slit region in all directions as a result the aspect ratio did not change.

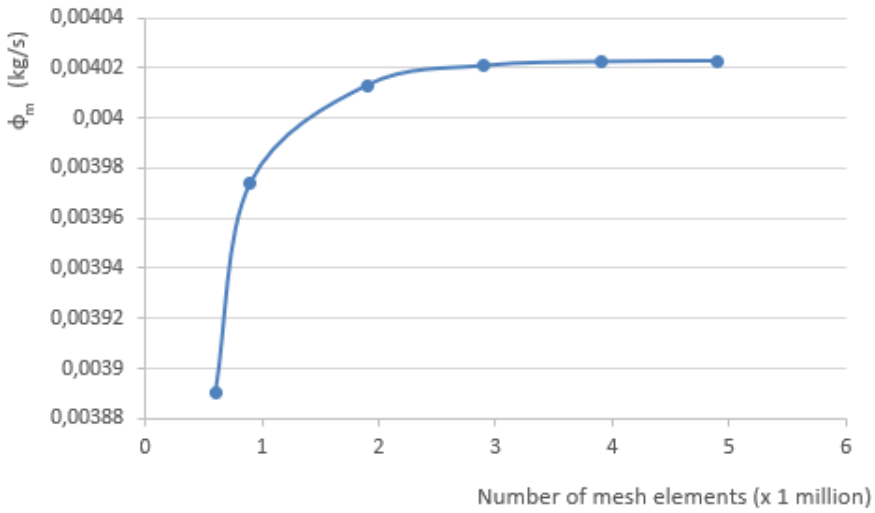

Figure 5.6: Optimization of mesh refinement

At 1.9 million elements the plateau is almost reached and therefore quite representative. This number is used in the first version of the model for now. However, the plateau starts around 3.0 million elements. To create the most accurate results without having an unnecessarily long run time 3.0 million elements is the optimum choice.

5.2. Final meshes

The final result, taken all the previous subsections into account, is a set of three hexahedral meshes for each of the three studied geometries, i.e. with slit widths of 2.0, 1.5 and 1.0 mm. The geometry is built with a box underneath the VDB where the outlet is placed at the vertical walls at the bottom of the box. In figure 5.7 the different parts of the mesh are shown clearly. The number of elements of the finest mesh is 1.9 million. This is not the optimum number but it is a good approach and will be used for the preliminary results in chapter 6. In figure 5.8 an example of one of the final meshes is shown. In table 5.1,5.2 and 5.3 the mesh quality of each of these meshes is given.

Mesh	# of cells (millions)	Mean orthogonality	% of aspect ratio below 1000
Base	0.6	0.86	100
Small	0.9	0.91	100
Tiny	1.9	0.95	100

Table 5.1: Mesh quality for a geometry with slit width 2.0 mm

Mesh	# of cells (millions)	Mean orthogonality	% of aspect ratio below 1000
Base	0.67	0.87	96
Small	1.0	0.91	100
Tiny	1.9	0.94	100

Table 5.2: Mesh quality for a geometry with slit width 1.5 mm

Mesh	# of cells (millions)	Mean orthogonality	% of aspect ratio below 1000
Base	0.67	0.87	100
Small	1.0	0.92	100
Tiny	1.9	0.95	100

Table 5.3: Mesh quality for a geometry with slit width 1.0 mm

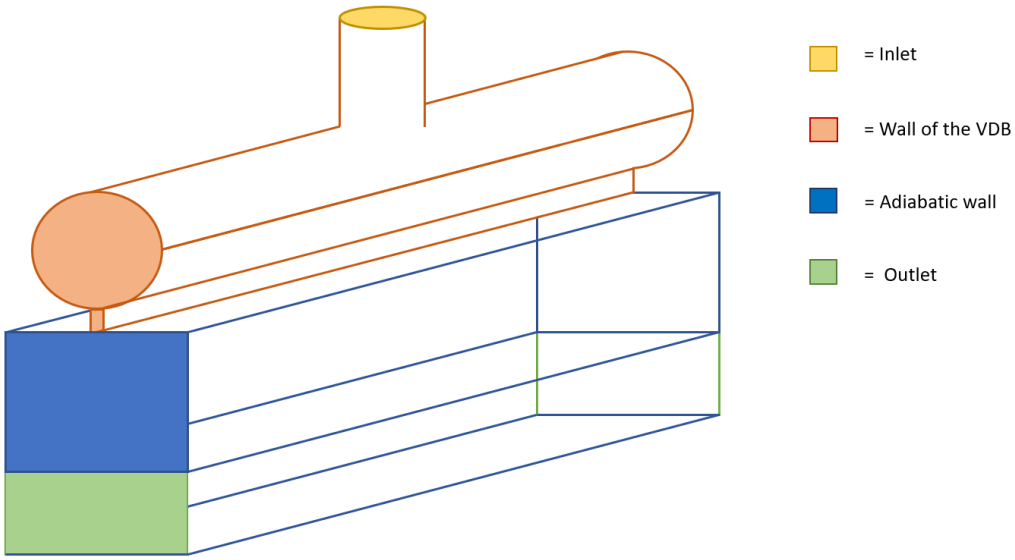

Figure 5.7: Definition of geometry parts

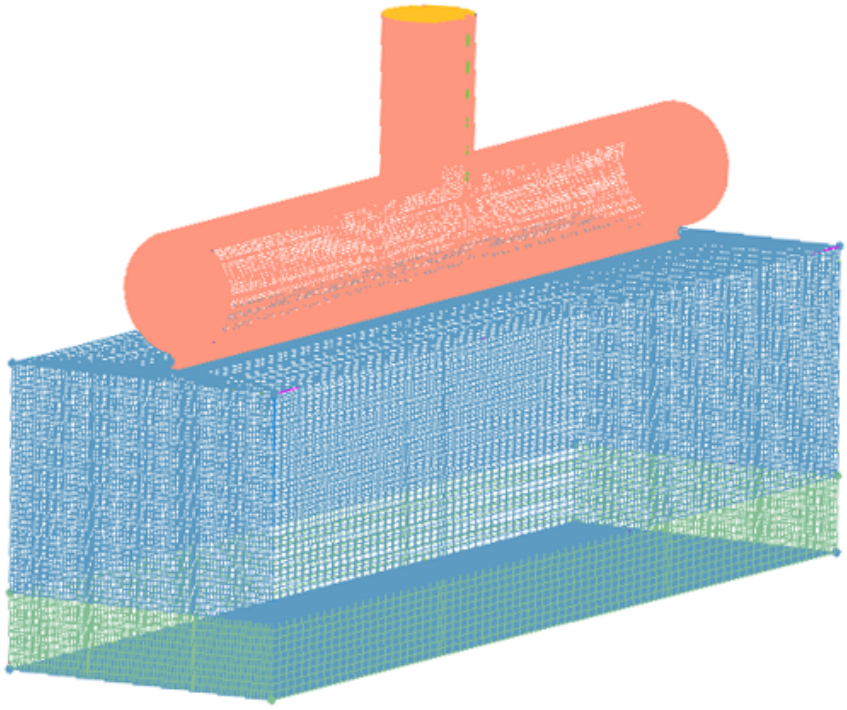

Figure 5.8: Final mesh

6

Results of the first version of the model

In this chapter the results are discussed. The presentation of the results is organized along four different objectives, each with their own hypothesis, method and results. In section 6.1 the results concerning the pressure and velocity contours are discussed. In the subsequent section, 6.2, the lateral distribution of mass outflow over the slit is analysed. In section 6.3 is analysed in which region of the VDB the phase state is above or below the vapour pressure curve to see whether it is likely for droplets to occur in these regions. Finally, in section 6.4 the influence of different slit widths is studied.

6.1. Pressure and velocity contours

This section will discuss the pressure and velocity contours in detail. First, a hypothesis is stated, next the method is described and finally the results are discussed on basis of the hypothesis.

Hypothesis

For the pressure contours the expectation is that virtually all the pressure drop should occur over the slit. The pressure inside the VDB is spread equally. For the velocity contours it is expected that the velocity field at the outlet becomes supersonic. Besides some recirculation profiles are expected as shown in figure 6.1. The Reynolds number will be in the critical zone between laminar and turbulent flow. Some recirculation is expected, but only in small regions.

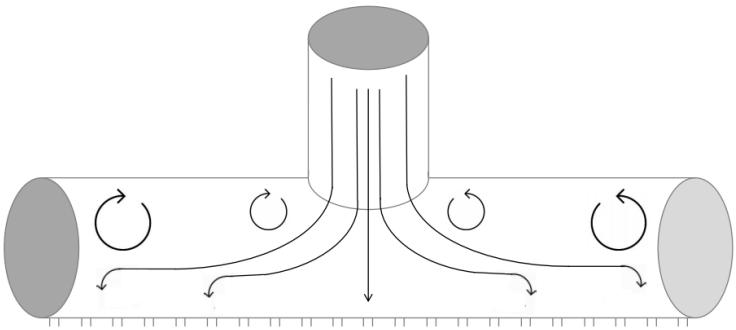

Figure 6.1: The expected re-circulation inside the VDB

Method

In ANSYS Fluent the graphics tool was used for post-processing the data. For the pressure and velocity contours the contour post-processing tool was used. For creating the recirculation the vector post-processing tool was used.

Results

The pressure contours meet the hypothesis. The pressure drop appears only over the slit and the pressure distribution is equal inside the VDB. In addition to the expected results, another phenomenon occurred; there is a little pressure stagnation zone at the centre of the slit, as shown figure 6.2.

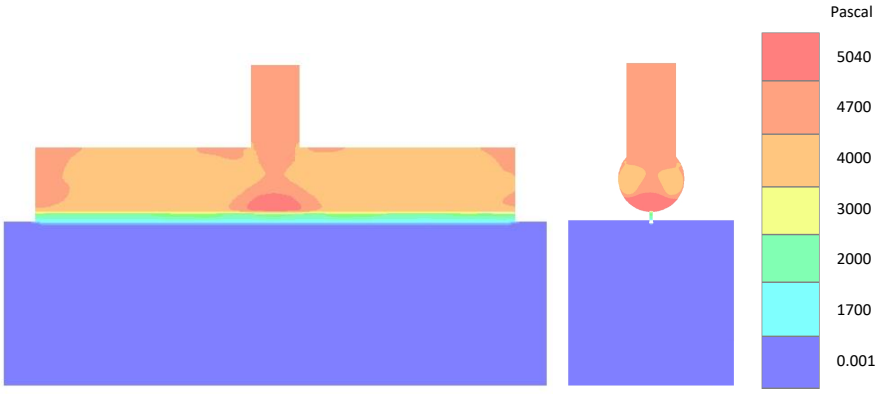

Figure 6.2: Static Pressure contour profile inside VDB

For the velocity field the contours are shown in figure 6.3. Over the long cross section a velocity decrease at the centre at the outlet is seen. This possibly indicates a shock inside the VDB. Since this research is interested in what happens inside the VDB itself and less about what happens after the slit a zoomed picture of the slit is shown in figure 6.4. The Mach number inside the slit is shown. The second light colors together form the supersonic region, which meets the hypothesis. However due to the shear of the walls the regions at the wall side are subsonic. This would results in a path for information to travel back where this is not possible in the supersonic region.

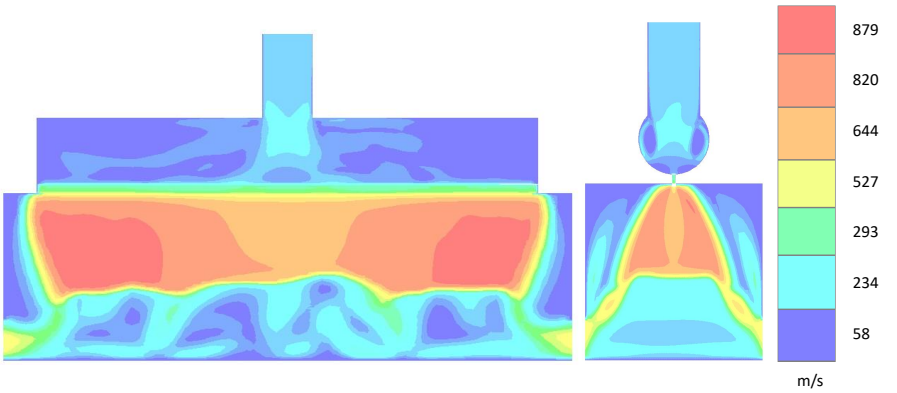

Figure 6.3: Velocity contour profile inside VDB

Figure 6.4: Mach number profile in the slit

Inside the VDB there is recirculation, as expected. The recirculation appears next to where the inlet enters, see figure 6.5. Further to the side the inertia forces will decrease and cause little to none recirculation in this zone. The high temperature has cause a relatively high viscosity and the flow pattern let believe us to be in the transition region between laminar and turbulent. In figure 6.6 it is shown that the Reynolds number lies between 80 and 240. For a flow perpendicular against a flat plate the transition region of the Reynolds number begins around 1000 [19]. From this men might conclude, looking at the vector contours, that the flow is in the turbulent region. However, since a steady-state simulation is performed and the chosen viscous model in Fluent is a laminar flow model, conclusions cannot be made regarding the nature of the flow pattern.

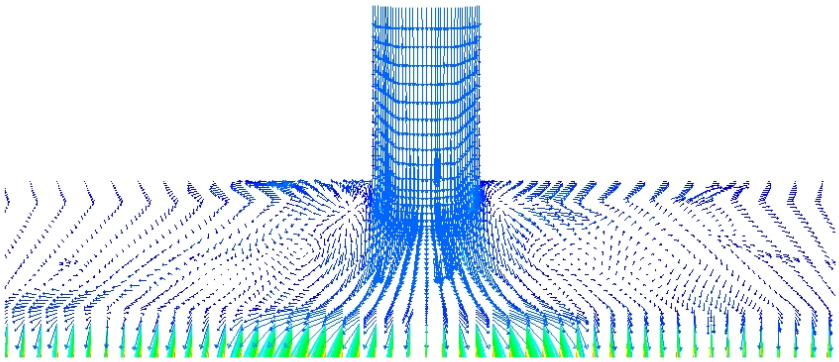

Figure 6.5: Recirculation shown by velocity vectors

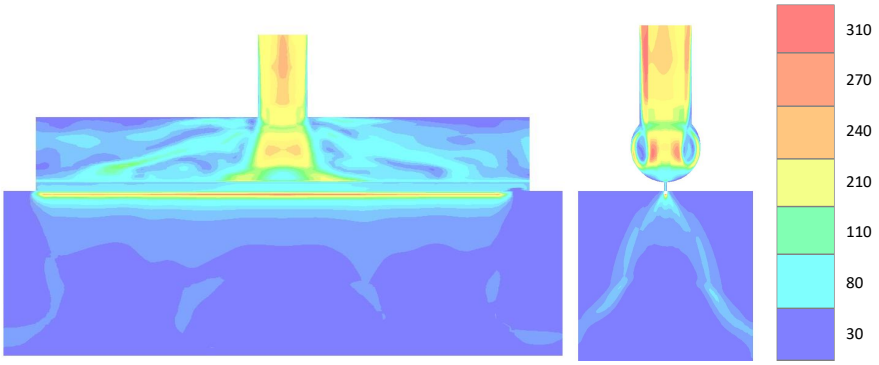

Figure 6.6: Reynolds number profile

6.2. Lateral distribution of mass outflow over the slit

In this section the lateral distribution of mass outflow of the slit is analysed. With the forthcoming researches taken in mind, it is important to control this mass outflow since this is of high impact on the path of the droplets that may occur.

Hypothesis

The lateral distribution of mass outflow over the slit is expected to be symmetric over the x-direction. At the centre there will be a peak. This is logically caused by a higher velocity at the centre of the VDB.

Method

The mass outflow is measured over the x-direction of the slit by dividing the slit into 20 different parts with each of a length of 0.015 m, shown in figure 6.7. For each of these faces the average mass flow rate is calculated. To get accurate results the mass outflow is taken at many iterations and are averaged again.

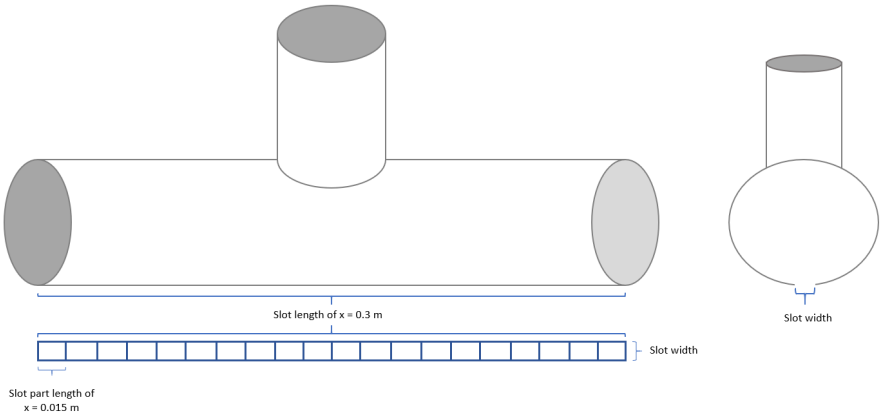

Figure 6.7: Slit divided in 20 parts

Results

In the following graph, 6.8, the results are shown. This curve is found for a geometry with slit width 1.0 mm and it is the mesh with the highest number of elements, 1.9 million.

The expected peak in the centre is appearing caused by the high velocity at the centre. Since the velocity towards the ends become stable a plateau is shown in the graph. In this graph a symmetry is

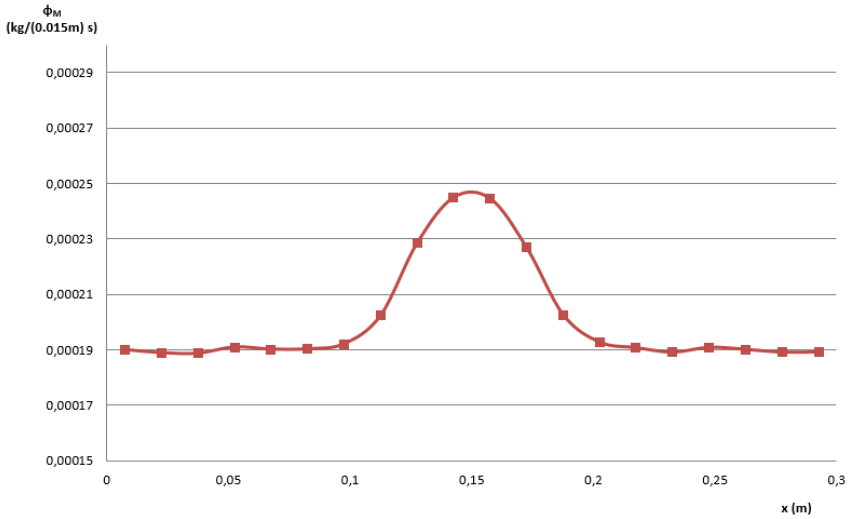

Figure 6.8: Mass outflow for a VDB with a slit of 2.0 mm wide, mesh: 1.9 million elements

clearly shown. There are two very small peaks at x=0.05 m and x=0.25 m. Why this peaks exists is not known. Further research has to be conducted to figure out what causes this little peaks.

6.3. Temperature pressure diagram to analyse in which regions the phase state is above or below the vapour pressure curve

This section will show if an approximation for the VDB outflow temperature and pressure based on an isentropic relation is feasible and this section will show in which regions of the VDB it is plausible for drops to occur. This will be predicted on the basis of the phase state of the regions.

Hypothesis

The heating from the wall of the VDB is so negligible that an approximation using an isentropic relation in feasible. For the saturation curve the following is expected. Since the walls are heated the temperatures at the wall regions are high. The more you get to the centre of the cylindrical tubes the more the phase state approaches the saturation curve. Since the pressure gradient inside the VDB is very small the temperature difference is decisive. Therefore the most likely region for the phase state to raise above the pressure curve is at the centre of the inlet cylinder.

Method

The isentropic relation for the inlet and outlet, pressure and temperature is given by

$$p = p_0 \left(\frac{T_0}{T} \right)^{\frac{\gamma}{(1-\gamma)}} \text{ [20] .} \tag{6.1}$$

An isentropic relation is only representative for isentropic processes, so adiabatic and reversible. For the PVD process we can assume it is reversible since the dissipation is negligible. On the other hand the process is not adiabatic because of the present heat transfer. To check whether the isentropic relation is valid for the PVD process the temperatures and pressure along a streamline are measured and put into equation 6.1 which needs to be fulfilled. The definition of a streamline is explained in chapter 3. Along a streamline, from the point at the inlet until the point at the slit outlet the temperature and pressure are not perfectly fitting the isentropic relation. Some streamlines fit the equation better than others. Therefore further research is needed to conclude whether the heating from the walls of the VDB is negligible and an approximation of the outflow temperature and pressure based on an isentropic relation is feasible.

For the saturation curve the following equation is used

$$\log p = -\frac{A}{T} + B + C \log T + 10^{-3} DT \text{ ,} \tag{6.2}$$

where the pressure, p, is in mmHg, A,B,C and D are constants, called the Antoine coefficients, and T is the temperature in Kelvin.[21]

A UDF, user defined function, is used to implement this equation in ANSYS Fluent. The UDF is fully displayed in appendix A. This UDF shows the vapour pressure for the local temperature and possible condensation regions, i.e. whether the local pressure is above or below the vapour pressure curve. It does not consider that the saturation curve is defined for temperatures in the range 473-1000K. Which means that the regions where T comes below 473 K need to be manually executed. The part between 473 K and 1000 K is split in half. Table 6.1 consists of Antoine coefficients applying to the two temperature ranges 473-692.5 K and 692.5-1000 K[21]. This Antoine coefficients are used in the UDF function and are component-specific constants.

Antoine coefficient	Temperature range 473-692.5 K	Temperature range 692.5-1000 K
A	6883.0	6670.0
B	9.418	12.0
C	-0.0503	-1.126
D	-0.33	0

Table 6.1: Antoine coefficients for different temperature ranges

Results

The results are shown for a geometry with slit width 2.0 mm. Number of elements of the mesh is 1.9 million. In figure 6.9 the vapour pressure for local temperatures is shown. in figure 6.10 is depicted in which regions the phase state is above and below the vapour pressure curve. Value 1 indicates a region above the vapour pressure curve. Value 0 indicates all regions below the vapour pressure curve. In figure 6.11 is shown which regions have a temperature below 473 K and are therefore not taken into account by the used system.

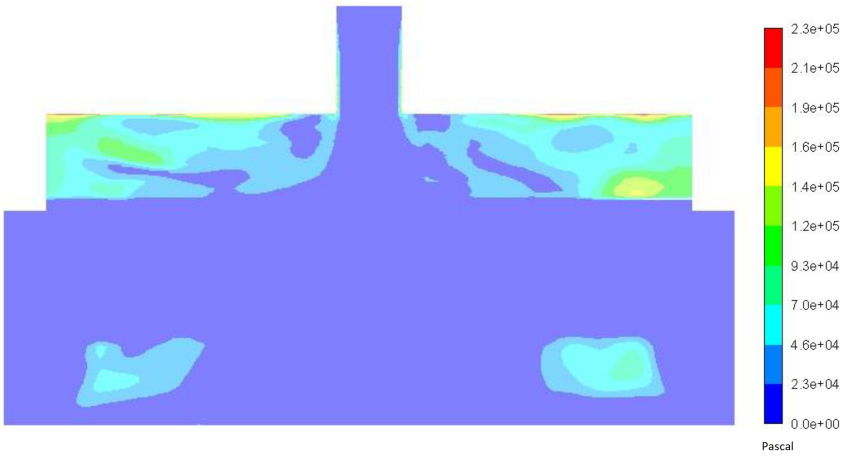

Figure 6.9: Contours of vapour pressure inside the VDB

The hypothesis can be stated as true. The centre of the inlet cylinder is the region where the phase is the closest to the vapour pressure curve. Additionally, the results show that the phase is actually above the vapour pressure curve.

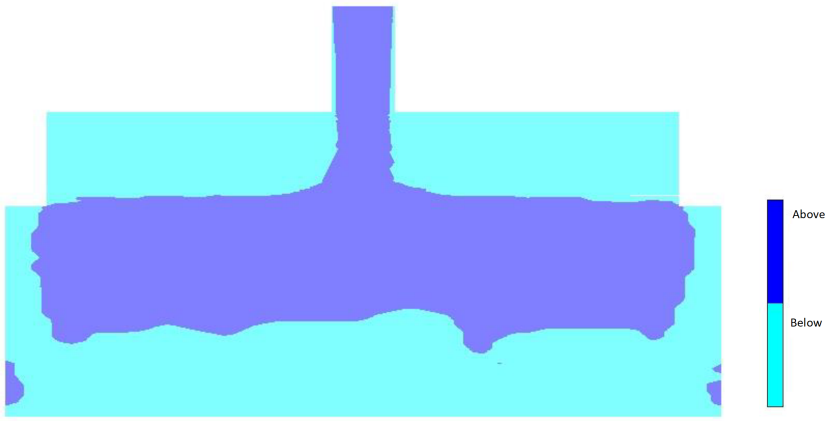

Figure 6.10: Region below and above the pressure curve

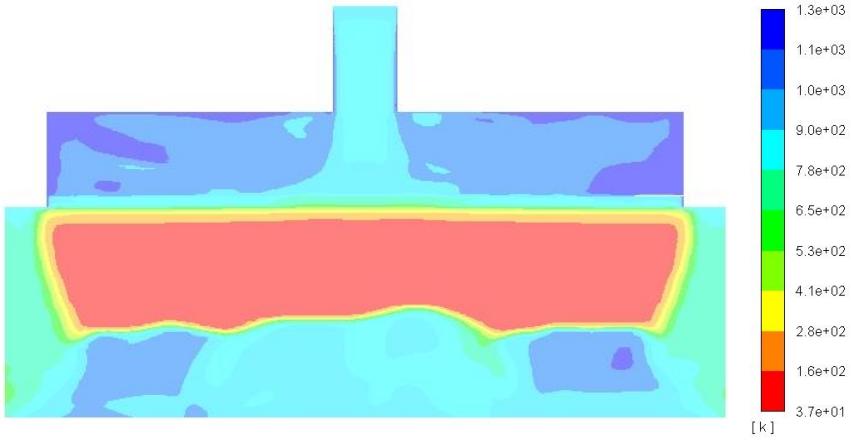

Figure 6.11: Temperature profile

6.4. The influence of different slit widths

In this section the influence of the different slit width on multiple variables is analysed. The difference caused by slit width will be analysed for all previous mentioned variables.

Hypothesis

- The pressure stagnation will decrease for a smaller slit
- The velocity will decrease at the inlet cylinder for smaller slits
- Reynolds will decreases for a smaller slit
- The mass outflow decrease with a decrease in slit width
- The regions where the phase state is above the saturation curve will negligible depend on slit width

Method

In ICEM CFD different geometry of the mesh were created by blocking. The geometry differ only in slit width. The three different slit widths that will be analysed are 1.0 mm, 1.5 mm and 2.0 mm.

Results

The pressure inside the VDB increases by a decrease in slit width. This is shown in figure 6.12. The pressure inside the VDB increases until equilibrium between the Zinc melt and Zinc vapour is reached.

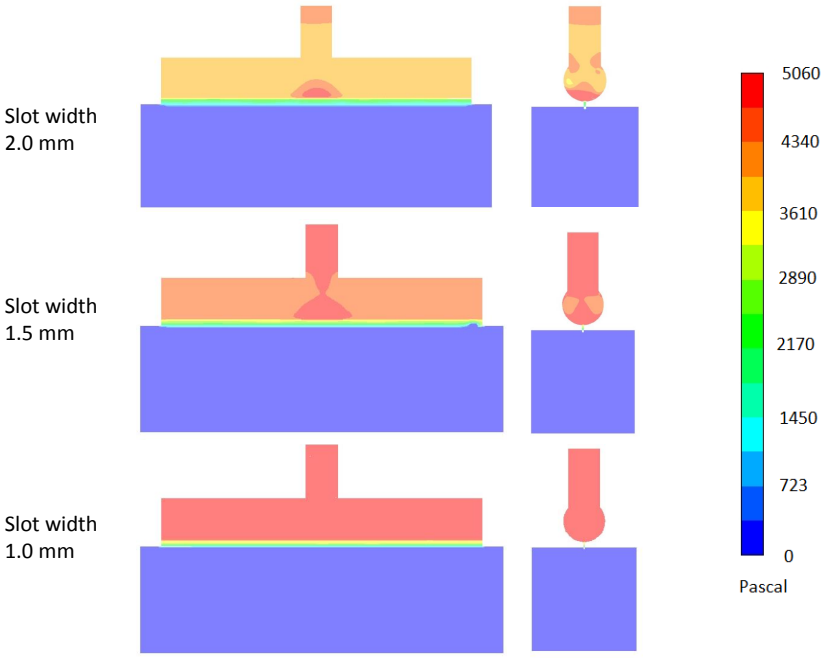

Figure 6.12: Pressure contours compared for three different slit widths

The velocity decreases at the inlet cylinder for smaller slits due to the outlet area decreasing whereby the flow cannot continue to stream at the same speed and will be held up. The confirmation of the hypothesis is shown in figure 6.13. By decreasing the slit width, the pressure inside the VDB will increase as well as the pressure gradient since the outlet pressure remains constant. Due to this increasing pressure gradient the velocity of the zinc vapour through the nozzle will increase.

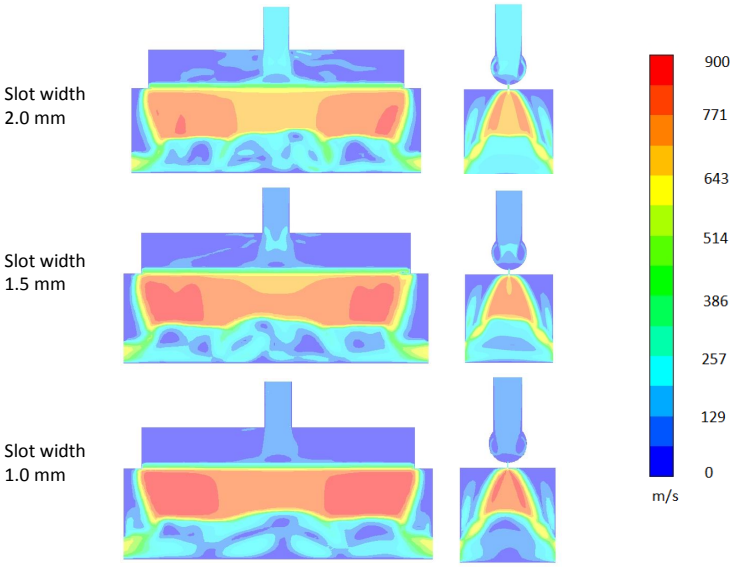

Figure 6.13: Velocity contours compared for three different slit widths

Reynolds increases for a wider slit due to increased velocities and an increasing characteristic length. This is shown in figure 6.14

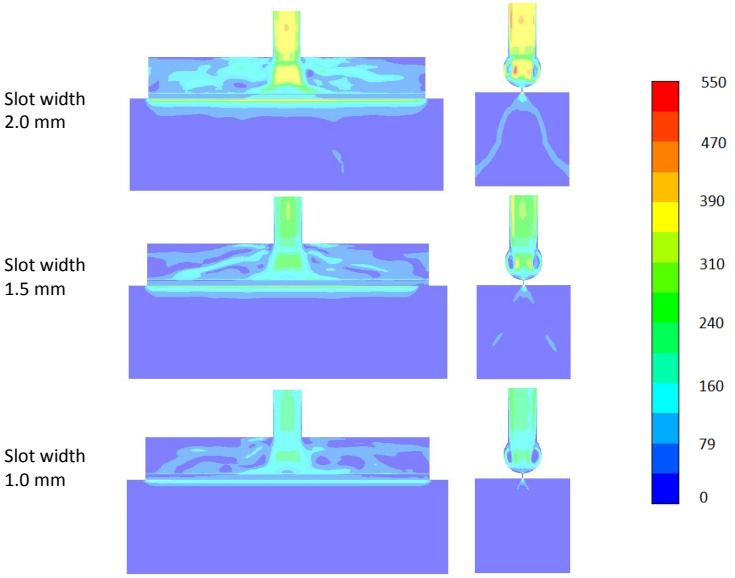

Figure 6.14: Reynolds contours compared for three different slit widths

The mass outflow decreases with a decrease in slit width. The area of the outlet decreases for smaller slit width. The little increase of the pressure gradient will increase the mass outflow. However this does not outweigh the large area change. With slit width 1.0mm, 1.5mm and 2.0 mm the total mass outflow is respectively 0.0018, 0.003 and 0.004 kg/s. The correlation between the slit width and total mass outflow is shown. The peak at the centre will flatten out. As seen in figure 6.15 for a slit width of 1.0 mm the peak is almost disappeared since the pressure ratio over the slit is the approximately same for every x.

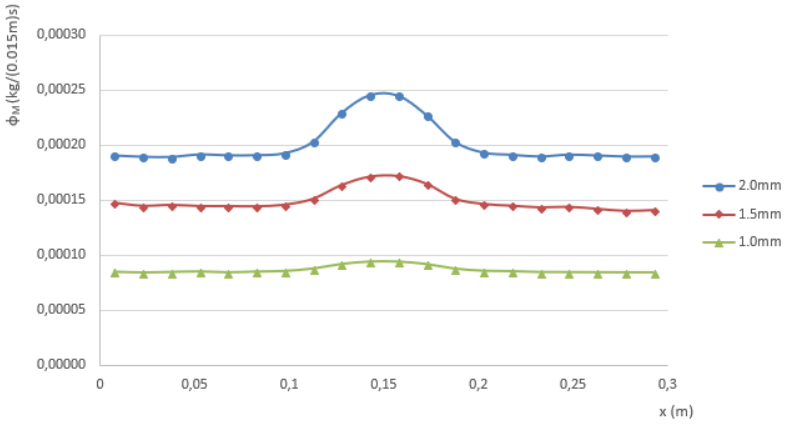

Figure 6.15: Lateral distribution of mass outflow over the slit for three different slit widths

The regions where the phase state is above the vapour pressure curve will not depend on slit width. This is confirmed in the result shown in figure 6.16. The temperature profile changes barely and the pressure change is to small to have an influence.

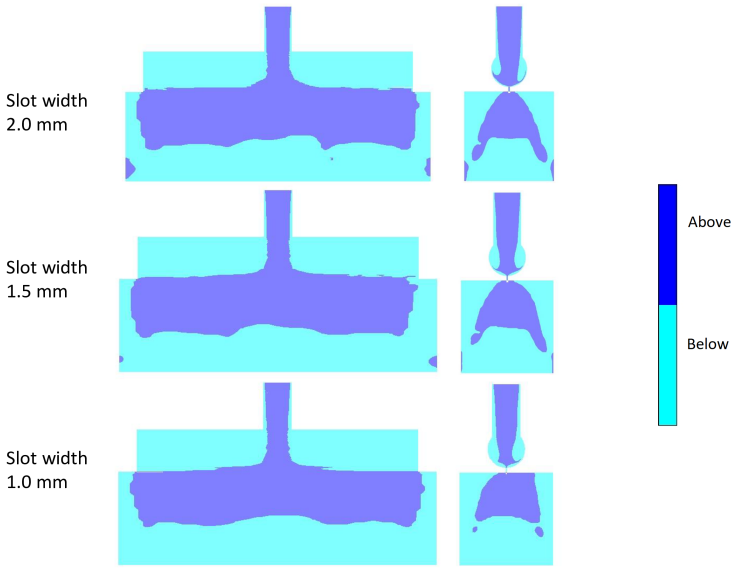

Figure 6.16: Regions above the vapour pressure curve for three different slit widths

7

Conclusion and recommendations

After this research conclusions can be made for each of the objectives. The first version of the model is a good base for further research. In section 7.2 is stated what improvements are still needed and what research can be performed when the model is finished.

7.1. Conclusions

- Sufficiently accurate results were reached with a Mesh containing 3.0 million elements.
- The mesh type needs to be hexahedral.
- The domain needs to be extended with a virtual box with an outlet at the sides to create valid boundary conditions.
- The slit region is subsonic at the wall region and therefore information is able to travel back.
- Recirculation occurs inside the VDB.
- The mass outflow shows two small, for now inexplicable, peaks which need further research.
- The isentropic relation is not yet proven to be feasible in this research.
- The centre region of the inlet cylinder is the region where the phase state is above the saturation curve and therefore the most likely region for droplets to occur.
- The slit width has a high influence on the pressure, velocity and Reynolds number inside the VDB.
- The increase in the total mass outflow is 1:1 correlated to an increasing slit width.
- The region where the phase state is above the saturation curve remains the same for different slit widths. The influence of the slit width is negligible.

7.2. Recommendations

The numerical model needs to be extended and improved. The following points needs to be carried out to achieve the final version of the numerical model:

- The geometry needs to be modified into an outlet with a certain number of nozzles.
- The number of elements needs to be scaled up to three million elements.
- The physical properties, like the thermal conductivity and viscosity, need to be adjusted with the exact numbers.
- A study on which viscous model is the most applicable.

When the final model is finished, it can be used to do research on the following objectives:

- Analyze the path of the droplets through the VDB.
- Analyze the evaporation and condensation of the droplets along their paths.
- Analyze the influence on the behavior of these droplets for different inlet conditions, as temperature and velocity.
- Analyze the influence on the behavior of these droplets for different nozzle diameters.

This analysis will lead to the understanding of the origin of the droplets and will lead to recommendations for the design of the VDB.

A

Appendix: User Defined Function

```
udf for t pressure
\#include "udf.h"

/*
This UDF shows, the vapour pressure for the local temperature and possible condensation
    regions,
i.e. whether the local pressure is above or below the vapour pressure curve.
It does not consider that the vapour pressure curve is defined for temperatures in the
    range 473-1000K.
*/

DEFINE\_ON\_DEMAND(calculateCondensationRegion)
{
        Domain *d;
        Thread *ct;
        cell_t ct;
        int k;
        real t,vp,ps,mmHgToPa;

        real A[]={6883.,6670.},B[]={9.418,12.},C[]={-0.0503,-1.126},D[]={-.33,0.};

        mmHgToPa=133.322368;
        d = Get\_Domain(1);
        thread\_loop\_c(ct,d)
        {
                begin\_c\_loop(c,ct)
                {
       t= C\_T(c,ct);

                        if (t<692.5)

                                { k=0; }

                        else

                                { k=1; }

                        vp=mmHgToPa*pow(10.,(-A[k]/t+B[k]+C[k]*log10(t)+0.001*D[k]*t));
                        ps = C\_P(c,ct) + op\_pres;/*static pressure + operating pressure
                            */

                        C_UDMI(c,ct,0) = vp; /* vapour pressure */

                        C\_UDMI(c,ct,1) = (vp<ps)?(TRUE):(FALSE);
                }
                end\_c\_loop(c,ct)
        }
}
```

Bibliography

[1] Anon., *World Steel in figures 2017*, Tech. Rep. (World Steel Association, 2017).

[2] E. Zoestbergen, T. Maalman, C. Commandeur, and M. Goodenough, *Influence of contamination on the thermal evaporation of a zinc melt,* Surface and Coatings Technology **218**, 108 (2013).

[3] S. Norris, *A Parallel Navier Stokes Solver for Natural Convection and Free Surface Flow* (University of Sydney. Engineering, 2000) pp. 7 – 51.

[4] J. Guerrero, *Introduction to computational fluid dynamics: Governing equations, turbulence modeling introduction and finite volume discretization basics,* State Key laboratory of Advanced Design and manufacturing for vehicle body (2014).

[5] J. Fan and I. Boyd, *Monte carlo modeling of electron beam physical vapor deposition of yttrium,* Journal of Vacuum Science & Technology **18**, 2937 (2000).

[6] G. K. Batchelor, *An Introduction to Fluid Dynamics* (Cambridge University Press, 2000).

[7] R. A. Granger, *Fluid Mechanics* (Dover Book, 1995).

[8] *ANSYS Fluent - CFD Software*, 17th ed. (ANSYS, Inc., 2016).

[9] ANSYS, *ANSYS Fluent Theory Guide*, 18th ed. (2017).

[10] J. John. D. Anderson, *Modern Compressible Flow with Historical Perspective*, 2nd ed. (McGraw-Hill inc., 1990).

[11] K. Dirks and M. Sharma, *Heat Capacity and Equipartition of Energy,* (2018).

[12] M. Schäfer, *Computational Engineering — Introduction to Numerical Methods* (Springer, Berlin, Heidelberg, 2006).

[13] *ANSYS ICEM CFD - Software*, 17th ed. (ANSYS, Inc., 2016).

[14] Shyam2791, *Types of mesh,* Wikipedia (2012).

[15] U. Hoffmann, A. Kloppel, A. Jischke, and P. Sauer, *(12) Patent Application Publication (10): US 2004/0163600 A1,* **1** (2004).

[16] J. A. F. M. Schade van Westrum, L. C. B. Baptiste, and G. Gleijm, *(12) Patent Application Publication (10) Pub . No .: US 2008/0280066 A1,* **1** (2008).

[17] ANSYS, *ANSYS CFX-Solver Modeling Guide*, 18th ed. (2017).

[18] ANSYS, *ANSYS Fluent User Guide*, 18th ed. (2017).

[19] L. Janssen and M. Warmoeskerken, *Transport phenomena data companion* (VSSD, 1987).

[20] G. van Wylen and R. Sonntag, *Fundamentals of Classical Thermodynamics* (John Wiley & Sons, 1965).

[21] E. Brandes and G. Brook, *Smithells metals reference book*, 7th ed. (Butterworth-Heinemann Ltd, 1992).